PHOTONICS Research

Optical fiber SPR biosensor complying with a 3D composite hyperbolic metamaterial and a graphene film

Can Li,[1] Jinjuan Gao,[1,2] Muhammad Shafi,[1] Runcheng Liu,[1] Zhipeng Zha,[1] Dejun Feng,[3] Mei Liu,[1] Xuejian Du,[1] Weiwei Yue,[1,2,4,5] and Shouzhen Jiang[1,2,6]

[1]Collaborative Innovation Center of Light Manipulations and Applications in Universities of Shandong School of Physics and Electronics, Shandong Normal University, Jinan 250014, China
[2]Shandong Key Laboratory of Medical Physics and Image Processing & Shandong Provincial Engineering and Technical Center of Light Manipulations, Jinan 250014, China
[3]School of Information Science and Engineering, Shandong University, Qingdao 266237, China
[4]Shandong Key Laboratory of Biophysics, Institute of Biophysics, Dezhou University, Dezhou 253023, China
[5]e-mail: yuewei@sdnu.edu.cn
[6]e-mail: jiang_sz@126.com

Received 4 December 2020; revised 13 January 2021; accepted 14 January 2021; posted 15 January 2021 (Doc. ID 416815); published 1 March 2021

In the present study, an optical fiber surface plasmon resonance (SPR) biosensor was developed for measuring time- and concentration-dependent DNA hybridization kinetics. Its design complies with a 3D Au/Al_2O_3 multilayer composite hyperbolic metamaterial (HMM), a graphene film, and a D-shaped plastic optical fiber. According to the numerical simulation and the experimental demonstration, the SPR peak of the designed biosensor can be effectively altered in the range of visible to near-infrared by varying the HMM structure. The sensitivity of the appliance was shown to achieve a value of up to 4461 nm/RIU, allowing its applicability for bulk refractive index sensing. Furthermore, a biosensor designed in this work displayed high-resolution capability (ranging from 10 pM to 100 nM), good linearity, and high repeatability along with a detection limit down to 10 pM, thus suggesting a vast potential for medical diagnostics and clinical applications.

https://doi.org/10.1364/PRJ.416815

1. INTRODUCTION

Surface plasmon resonance (SPR) currently turns out to be one of the most feasible techniques for developing biological sensors for label-free, point-of-care, and high-throughput applications [1–7]. The resonance results from the coherent free electron oscillations that are propagated along the metal/dielectric interface when the wave vector satisfies the momentum matching conditions [8]. Typical metals used for SPR applications are gold and silver [9–11]. Owing to their highly sensitive electromagnetic field associated with the mentioned oscillations, the SPR exhibits a noticeable sensitivity to the refractive index (RI) of the surrounding dielectric material.

Conventional SPR sensors possess the built-in Kretschmann configuration, which strongly depends on large optical components, thereby resulting in high operational costs and difficulty in miniaturization in the fields of precision medicine and system biology [12–14]. In this regard, the emerging optical fiber that exhibits numerous prominent features (e.g., low cost, lightweight, ease of use, long-distance sensing, and small dimensions) can be employed for developing state-of-the-art SPR sensors [5,6,15–17]. Thus far, meaningful works have been performed to improve the already existing optical fiber SPR sensor configuration by applying optical fibers. Given the detection area morphology, fiber-optic SPR sensors can be D-shaped [18], U-shaped [19], tapered [20], or take other forms [21]. Among these, the D-shaped sensing probe has a range of benefits (e.g., high sensitivity, easy functional modification, and wide detection area). As for optical fiber materials, plastic optical fiber (POF) has aroused attention due to its super machinability and handling along with low cost [22–24].

So far, tremendous effort has been made to boost the development of optical fiber SPR sensors. In 2018, Gong *et al.* proposed a novel D-shaped optical fiber SPR sensor based on the graphene/Au hybrid structure with a sensitivity of 1227 nm/RIU for DNA hybridization detection [25]. In 2019, by depositing a Cu-nanoparticle/carbon nanotube composite film onto the gold film, Zhang *et al.* obtained a reflective fiber

optic SPR sensor for simultaneous measurement of nitrate concentration and temperature [21]. In 2020, seizing the advantages of photonic crystal fibers, Wang *et al.* developed an ultra-wide detection range refractive-index SPR sensor with a sensing range of 1.29–1.49 [26]. In 2020, using glucose oxidase as a sensitive film covalently bonded on the gold film, Zheng *et al.* designed a highly sensitive and reflective glucose SPR sensor to measure glucose concentrations [27]. However, a leap forward in clinical applications toughened requirements for the sensitivity and stability of optical fiber SPR sensors.

Over the past few years, rapid progress in the micro/nano processing technology enabled the experimental demonstration of various artificial optical metamaterials, whose magnetic properties were improved compared to conventional materials [28]. In this respect, hyperbolic metamaterials (HMMs) have rapidly gained a central role due to their capability to access and manipulate the near field of a light scatterer or a light emitter, which derives directly from the excitation, within HMMs, of coupled surface plasmons [8,29]. HMMs refer to uncommon artificial electromagnetic metamaterials that display hyperbolic dispersion with bulk 3D sub-wavelength structures that are anisotropic in permittivity. Recently, extreme sensitivity has been achieved by employing HMMs [30–32]. In 2009, Kabashin *et al.* proposed a plasmonic nanorod metamaterial for high-sensitivity plasmonic biosensors with sensitivity to RI variations of more than 30,000 nm/RIU using a prism-coupling mechanism [33]. In 2016, Kandammathe *et al.* developed a miniaturized plasmonic biosensor platform based on a hyperbolic metamaterial of a three-dimensional multilayer metal (Au/Al_2O_3) and unconventional two-dimensional gold diffraction gratings, allowing sensitivity of up to 30,000 nm/RIU [34]. Furthermore, the angular scans with extraordinary angular sensitivity of 7000° per RIU were achieved in a visible-to-near-infrared (NIR) wavelength range [35]. However, the complex system configurations bring some limitations to the mentioned biosensors, such as insufficiency to address high costs and difficulty in miniaturization.

In this respect, the present work is aimed at designing an SPR optical fiber biosensor based on a 3D Au/Al_2O_3 composite HMM, a graphene film, and D-shaped plastic optical fiber (D-POF) (G/HMM/D-POF). The performance of the setup was assessed via numerical simulation and experimental demonstration. Compared with a conventional fiber optic SPR sensor, introducing the multilayer HMM was shown to considerably improve the sensitivity of the appliance under consideration. Furthermore, graphene was proved to enhance the performance of a biosensor in three aspects: sensitivity, molecular affinity, and stability [36–39]. Under the D-type fiber structure, the position of the SPR resonance peak could be effectively tuned in the range of visible to NIR by altering the structure of HMM. The G/HMM/D-POF sensor proposed in this study exhibits a set of advantages, such as simple fabrication and low cost along with high sensitivity (4461 nm/RIU), good stability, linearity, and repeatability. Furthermore, in the aspect of biological detection, the SPR biosensor was successfully applied for measurement of time- and concentration-dependent DNA hybridization kinetics, which demonstrated excellent performance.

2. MATERIALS AND METHODS

A. Materials

The graphene-oxide dispersion was provided by Xianfeng Nano Technology Co., Ltd. A 50% hydrazine hydrate solution (N_2H_4) and poly(allylamine hydrochloride) (PAH, C_3H_8ClN) were purchased at China Pharmaceutical Co., Ltd. In addition, the 1-pyrenebutanoic acid succinimidyl ester (PBASE), dimethyl sulfoxide (DMSO), and phosphate-buffered saline (PBS, P5368-10PAK) were offered by Sigma-Aldrich Co. (Shanghai, China). The DNA (Table 1) was purchased at Sangon Biotech Inc. (Shanghai, China). Finally, the probe aptamer, mis_DNA, and t_DNA solutions with different concentrations were produced and diluted in a PBS buffer solution to be applied, as well.

B. Preparation of D-POF

A 1-mm-thick plastic optical fiber working in a wavelength range of 450–840 nm was adopted as the probe substrate of the SPR sensor. First, it was cut into 15-cm-long strips. Second, in the middle of the optical fiber section, the cladding and part of the fiber core were removed by the side polishing to obtain sensing areas with 1.5-cm lengths. Last, the D-POF was cleaned with de-ionized (DI) water to remove surface impurities.

C. Preparation of G/HMM/D-POF

The synthesis of G/HMM/D-POF is illustrated in Fig. 1. A series of composite HMMs was produced by the sequential deposition of gold and Al_2O_3 layers so that the Al_2O_3 layers split the gold film into n different layers ($n * Au/Al_2O_3$), where n varied from 2 to 5, respectively. Since the functional layer thickness in the conventional single-layer gold SPR sensor is between 30 and 80 nm, with an optimum thickness of 50 nm [40–42], the total gold layer thickness in the HMM was set at 50 nm to study more intuitively the enhancing effect of HMM. The thickness of the entire functional layer was compressed under 80 nm. First, the gold layer was deposited on the top of the POF via thermal evaporation of gold pellets at a rate of 0.7 $Å \cdot s^{-1}$ (1 Å = 0.1 nm). Accordingly, a 6-nm-thick Al_2O_3 layer was applied onto the gold film by the oxidation of the metal aluminum [43], and so on. In order to enhance the effect of graphene on the surface plasmon resonance, the uppermost HMM layer was the gold layer. The ratio of metal to dielectric thicknesses per unit period is critical to HMMs [44]. Among the mentioned structures, the optimum candidate (HMM/POF) was selected for graphene growth and biological modification in the next step. For comparison, a conventional SPR sensor based on a single-structure 50-nm-thick gold film (Au/D-POF) was designed, as well.

In turn, a multilayer graphene structure was capped with the HMM/D-POF surface through the 1-h immersion in PAH

Table 1. DNA Applied in This Study

Type	Sequences (15-mers)
Probe aptamer	5′-TGT ACA TCA CAA CTA-3′
Target DNA	5′-TAG TTG TGA TGT ACA-3′
Mis_DNA	5′-CCT CCA CAG CTC GAG-3′

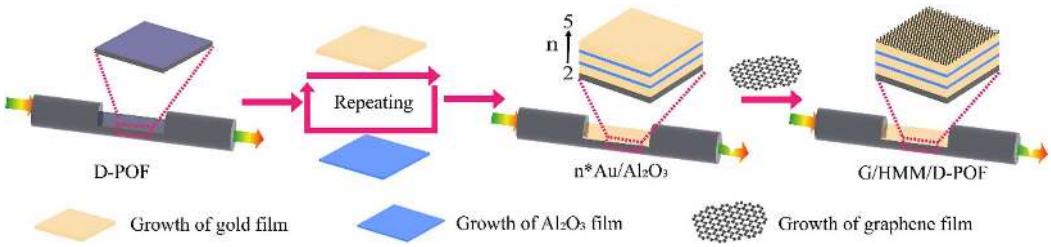

Fig. 1. Preparation process of G/HMM/D-POF.

solution ($1\ g \cdot L^{-1}$), and subsequent reactions with a graphene-oxide dispersion ($0.2\ g \cdot L^{-1}$; flake diameters of 50–150 nm) for 5 h and hydrazine (N_2H_4, 50%) for 1 h [45,46]. After that, the obtained G/HMM/D-POF structure was washed with DI water and dried with nitrogen.

D. Modification and DNA Detection

In order to modify the G/HMM/D-POF for DNA detection, the obtained sensor was immersed in a 1 μM (1 M = 1 mol/L) PBASE solution for 4 h [38,47]. The pyrene group of the PBASE could undergo $\pi - \pi$ stacking with graphene and succinimide conjugate with an $-NH_2$ group-modified aptamer probe. The unmodified PBASE was removed by triple washing with DMSO and de-ionized water. After that, on the G/HMM/D-POF surface, the probe aptamer with $-NH_2$ was fixed by inserting the sensor into the solution (1 μM) for 4 h. Subsequently, the probe was rinsed with a PBS solution and de-ionized water to remove the unreacted probe aptamer. Finally, the modified G/HMM/D-POF sensor could be employed to perform the detection of DNA hybridization. The performance of the sensor proposed in this study was assessed using t_DNA and mis_DNA solutions of various concentrations. Before each detection, the sensor was cleaned with a PBS solution. For the DNA dissociation dynamics, the relevant solution was replaced with a pure 0.01× PBS buffer to remove target DNAs. The dissociation was ended via a 60-s immersion of 10-mM aqueous sodium hydroxide solution and rinsing with PBS solution. Furthermore, the entire reaction was monitored in the real-time mode through the transmission spectrum.

E. Experimental Setup

An experimental setup for analyzing the performance of a designed G/HMM/D-POF sensor is illustrated in Fig. 2. The sensor was fixed in the polyethylene (PE)-based reaction cell (length: 2 cm, diameter: 5 mm), which was designed specifically for probe solution detection. The SPR peak shifts were recorded with a PG2000 fiber optic spectrometer (Ideaoptics Instruments), and an Ocean Optics HL-2000 tungsten lamp emitting in a wavelength range of 360–2000 nm served as an excitation light source. The surface morphology of 3D nanostructures was characterized using a Zeiss Gemini Ultra-55 scanning electron microscope (SEM).

3. RESULTS AND DISCUSSION

HMMs refer to a class of attractive artificial materials that exhibit the feature of hyperbolic dispersion $[\omega^2/c^2 = (k_x^2 + k_y^2)/\varepsilon_z + k_z^2/\varepsilon_x]$ with the property that their principal permittivity components have the opposite sign to the other two ($\varepsilon_x = \varepsilon_y$ and $\varepsilon_x \times \varepsilon_z < 0$) [48,49]. Since in this study, the thicknesses of the individual metal or dielectric layers composing the $n * Au/Al_2O_3$ structures were far below the excitation wavelength, the effective medium theory was adopted to calculate the dielectric permittivity tensor components [50]. In this regard, Fig. 3(a) displays the real and imaginary parts of the in-plane ε_x and out-of-plane ε_z permittivity components for the $n * Au/Al_2O_3$ structure with $n = 3$ versus excitation wavelength. An obvious hyperbolic dispersion is observed at $\lambda \geq 580$ nm, where $\varepsilon_x < 0$ and $\varepsilon_z > 0$. For the structures with other n values, the relevant wavelengths associated with hyperbolic dispersion were 630 nm ($n = 2$), 550 nm ($n = 4$), and 540 nm ($n = 5$), respectively [Fig. 3(b)].

Furthermore, the finite difference time domain (FDTD) method was employed to demonstrate the different sensitivities to RI variations of HMMs with different n values. For comparison, this study collected the performance of conventional SPR sensors exhibiting the structure of only one 50-nm gold film (Au/D-POF). The simulation setup is illustrated in Fig. 3(c). TM-polarized light with a 72° angle of incidence was adopted as the excitation source. Figure 3(d) displays the normalized transmission spectra of Au/D-POF and $n * Au/Al_2O_3$ systems for the bulk RIs ranging from 1.340 to 1.352. As seen, compared with a transmission spectrum of Au/D-POF at the RI of 1.340, the resonant peak values

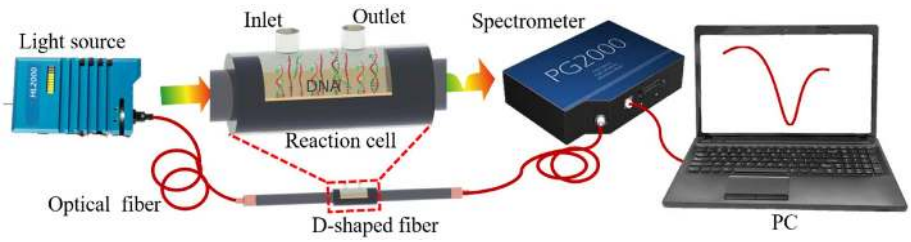

Fig. 2. Schematic of an experimental setup based on the G/HMM/D-POF sensor.

associated with $n * Au/Al_2O_3$ structures exhibit a pronounced redshift, and the morphology was broadening with increasing n value. According to the quantitative assessments from Fig. 3(d), the redshift observed for $n * Au/Al_2O_3$ with changing RI from 1.340 to 1.352 increases from 44 to 54 nm and the resonance peak wavelength at the RI of 1.340 is altered from 683 to 723 nm [Fig. 3(e)]. The full width at half-maximum for Au/D-POF and $n * Au/Al_2O_3$ ($n = 2$–5) at the RI of 1.340 in Fig. 3(d) is 57.52, 57.76, 58.22, 59.26, and 60.96 nm, respectively. The broadening of the resonance peak with increasing n can be explained in terms of the imaginary part of the dielectric constant [Fig. 3(a)]. For pure gold, a monotonic increase in the imaginary part for the wavelengths above 470 nm caused a narrow SPR resonance at lower wavelengths.

For $n * Au/Al_2O_3$, a feature similar to a concave protuberance existed in the spectrum of the imaginary part in the dielectric constant, thereby allowing more wavelengths to approach the SPR resonance and causing the broadening and redshifting of the relevant resonance peaks in Fig. 3(d). Furthermore, a periodical stacking of sub-wavelength metal/dielectric layers makes the electromagnetic fields bounded at the individual plasmonic interfaces further contribute to a collective response, thus acting as the source of HMMs' super sensitive property [48,51]. In this respect, the electric field distributions within Au/D-POF and $n * Au/Al_2O_3$ structures at the resonance wavelengths for the RI of 1.340 are illustrated in Fig. 3(f). The emergence of periodic oscillations along with a substantial increase of the resulting electric field with increasing n is likely due to the coupling between the electromagnetic waves bounded at the individual plasmonic interfaces. Subsequently, the alteration curves of the electric field norm with physical depth in each distribution were integrated [Fig. 3(g)].

The obtained Au/D-POF and $n * Au/Al_2O_3$ structures are depicted in Fig. 4(a). All the sensors developed in this study exhibited good uniformity and repeatability in appearance. Figure 4(b) displays the top SEM image of the $3 * Au/Al_2O_3$ structure. An obviously smooth HMM surface facilitates the SPR excitation and results in a higher signal-to-noise ratio. Figures 4(c) and 4(d) display the SEM cross-sectional images of a 50-nm-thick gold structure and a $3 * Au/Al_2O_3$ system. Because of the strong flexibility of POF, the samples were placed onto the silicon substrates to ensure their more accurate morphological characterization. In these SEM images, the bright layers refer to the gold film and the dark ones are attributed to the Al_2O_3 layers. It is clearly seen that the 6-nm-thick Al_2O_3 layers provide the effective bilateral isolation of the gold layers, which is crucial for the HMM design. Thus, a periodically stacked sub-wavelength Au/Al_2O_3 structure ensures the bounding and coupling of the electromagnetic fields between the individual plasma interfaces. The energy dispersive spectrometer (EDS) results visualized in Figs. 4(e)–4(h) evidence the successful construction of the Al_2O_3 spacer layer.

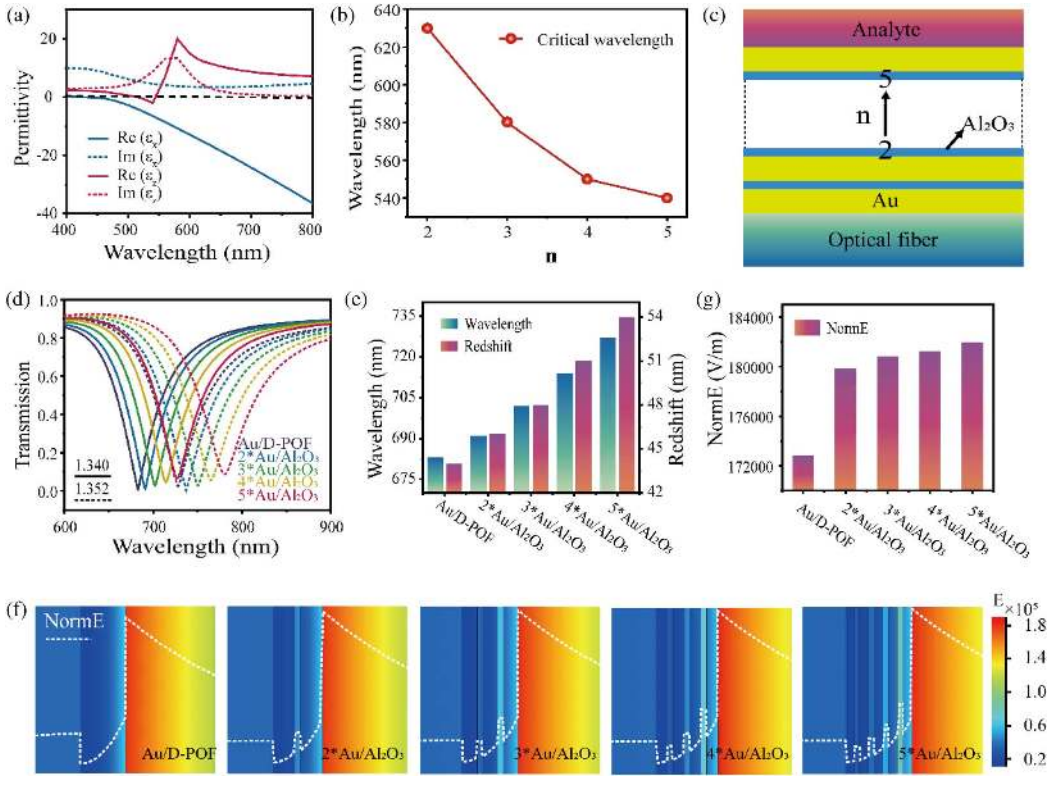

Fig. 3. Simulation results. (a) Real and imaginary parts of the in-plane ε_x and out-of-plane ε_z permittivity components for an $n * Au/Al_2O_3$ structure with $n = 3$. (b) Critical wavelength for $n * Au/Al_2O_3$ structures as a function of n value. (c) Simulation setup of the structure $n * Au/Al_2O_3$ ($n = 2$–5). (d) Normalized transmission spectra of Au/D-POF and $n * Au/Al_2O_3$ ($n = 2$–5) for RI increasing from 1.340 to 1.352, respectively. (e) SPR peak wavelengths at the RI of 1.340 and their redshifts at RIs varying from 1.340 to 1.352 for Au/D-POF and $n * Au/Al_2O_3$ ($n = 2$–5). (f) Electric field distributions within Au/D-POF and $n * Au/Al_2O_3$ ($n = 2$–5) structures at the resonance wavelengths for the RI of 1.340. (g) NormE values for Au/D-POF and $n * Au/Al_2O_3$ ($n = 2$–5).

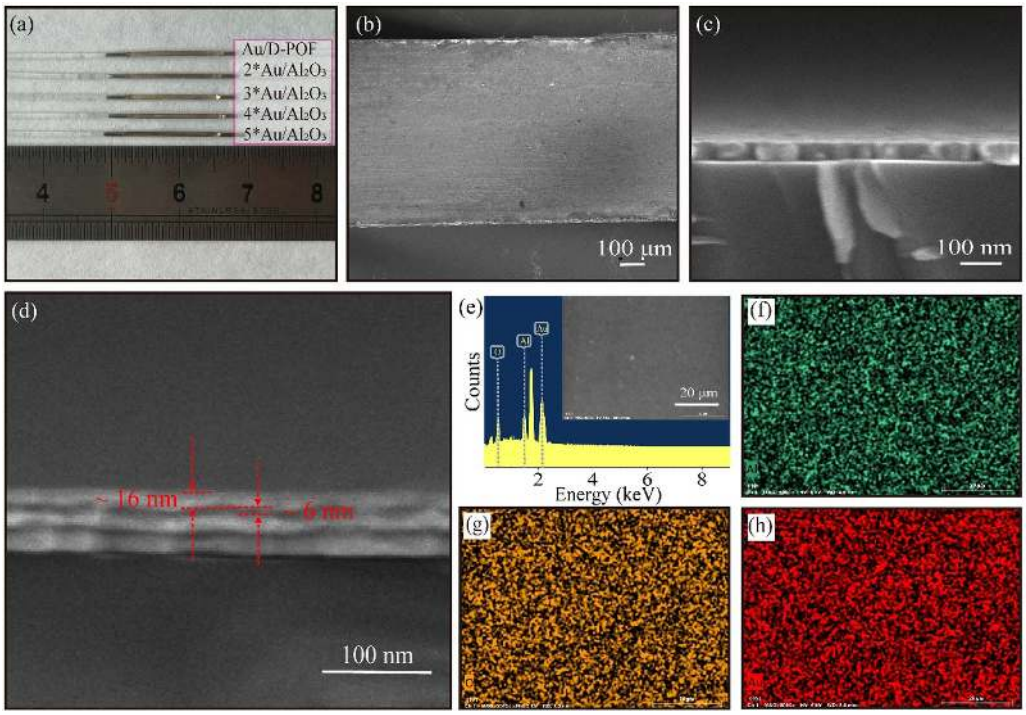

Fig. 4. (a) Optical graph of Au/D-POF and $n * \mathrm{Au/Al_2O_3}$ ($n = 2$–5). (b) Top SEM image of $3 * \mathrm{Au/Al_2O_3}$. (c) SEM cross-sectional image of a 50-nm-thick gold structure. (d) SEM cross-sectional image of $3 * \mathrm{Au/Al_2O_3}$. (e) EDS spectra of $3 * \mathrm{Au/Al_2O_3}$. (f)–(h) EDS element distribution maps from (f) Al, (g) O, (h) Au on $3 * \mathrm{Au/Al_2O_3}$.

In order to compare the bulk refractive index detection capabilities of Au/D-POF and $n * \mathrm{Au/Al_2O_3}$ ($n = 2$–5), the next step was to study the performance of both types of sensors in ethanol solutions. Figures 5(a)–5(e) display the normalized transmission spectra of Au/D-POF and $n * \mathrm{Au/Al_2O_3}$, acquired in the ethanol solutions with RIs from 1.340 to 1.352. As seen, the experimental data exhibit a trend similar to that obtained by the numerical simulation in Fig. 3(d). Compared with a transmission spectrum of Au/D-POF, there is a pronounced alteration of the SPR peaks from 629.67 to 732 nm along with their broadening for $n * \mathrm{Au/Al_2O_3}$ structures at RI of 1.340. Furthermore, the redshift increases from

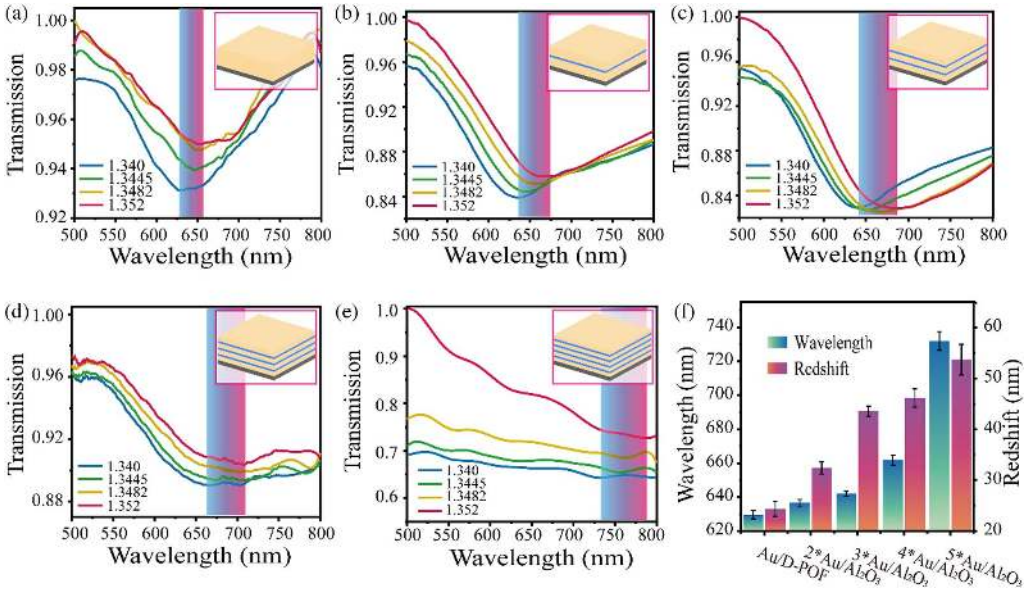

Fig. 5. (a)–(e) Normalized transmission spectra of Au/D-POF and $n * \mathrm{Au/Al_2O_3}$ ($n = 2$–5) in the ethanol solution with RIs ranging from 1.340 to 1.352, respectively. (f) SPR peak wavelengths for Au/D-POF and $n * \mathrm{Au/Al_2O_3}$ ($n = 2$–5) in the ethanol solution at the RI (1.340) and the redshifts caused by increasing RI (from 1.340 to 1.352).

24.4 to 53.66 nm, with increasing RI of 1.340 to 1.352. The alteration curves of SPR peak wavelengths and redshift values are summarized in Fig. 5(f). It is noteworthy that, on the one hand, at n reaching a value of 4 or 5, the strong resonance coupling between the bilayers under the limit size dramatically improves the sensitivity of the sensor. On the other hand, such a pronounced SPR peak broadening increases the noise, thus reducing the resolution of the sensor. Moreover, within the operating wavelength range of the POF, the excessively shifted resonance wavelength could not ensure sufficient space for the next stage of graphene growth and biological modification and detection. For this reason, the priority for further study is given to a $3 * Au/Al_2O_3$ structure.

Thus, a G/HMM/D-POF system was obtained by depositing the multilayer graphene on the top of the $3 * Au/Al_2O_3$ structure by the chemical method described in Section 2.C. Graphene, as part of a sensor, has three primary functions. First, the 2D honeycomb lattice of carbon atoms with sp^2 structure and a large surface area ($\sim 2630\ m^2 \cdot g^{-1}$) ensures high molecular affinity [38]. Second, the graphene layer strengthens the electric field of surface plasmon polaritons, thereby facilitating the interaction between biomolecules and the evanescent field [11,25]. Third, graphene exhibits prominent chemical inertness, effectively improving the stability and service lifespan of the sensor [39]. Figure 6(a) displays the SEM image captured on the front of the sensing area of the G/HMM/D-POF. The presence of a graphene film is obvious from the blurred wrinkles on the gold layer surface. Furthermore, compared with the characteristic peaks of graphene oxide in Raman spectra, the peak at 2905 cm^{-1} verified the construction of graphene film deposited on the $3 * Au/Al_2O_3$ in Fig. 6(b). Immediately afterward, the normalized transmission spectrum of the G/HMM/D-POF system was collected in the ethanol solutions with RIs from 1.340 to 1.352. The redshift of the SPR resonance peak wavelength could reach a value of 53.53 nm, meaning a sensitivity of 4461 nm/RIU. Thus, compared with $3 * Au/Al_2O_3$ (3627.5 nm/RIU), the sensitivity of the G/HMM/D-POF sensor has significantly been improved. Figure 6(d) illustrates the relationship between the wavelength redshift of G/HMM/D-POF as a function of RI. Obviously, it follows the linear behavior, and the fitting with a straight line results in a high coefficient of determination (R^2) of 0.996. This indicates the excellent linear detection capability of the G/HMM/D-POF. Figure 6(e) shows the normalized transmission spectra acquired under identical conditions (RI of 1.352) in a cycling mode (up to 10 cycles) to characterize the reproducibility of a sensor. The uniform profiles of the spectra allow one to suggest the outstanding reproducibility properties of the designed G/HMM/D-POF sensor. Besides this, Fig. 6(f) displays the typical response-recovery characteristic of a sensor with RI = 1.352 at a resonance wavelength of 648 nm. Once immersed in the ethanol solution, the absorbance increases to 10% within ~0.9 s. Such an excellent response-recovery ability could result from the high surface-to-volume ratio due to the applied graphene film. In this respect, the mentioned characteristics proved the excellent performance of a G/HMM/D-POF sensor designed for bulk refractive index detection.

The capability of a designed G/HMM/D-POF sensor to be used for the biomolecule detection was assessed by measuring the time- and concentration-dependent DNA hybridization kinetics. Such a technique is essential for genetic screening and transcriptional profiling, as well as for the detection of biomarkers and single-nucleotides variants. Modified, bonded, and dissociated DNAs were detected and analyzed by monitoring the normalized transmission spectra. Figure 7(a) shows the normalized transmission spectra evolving with DNA

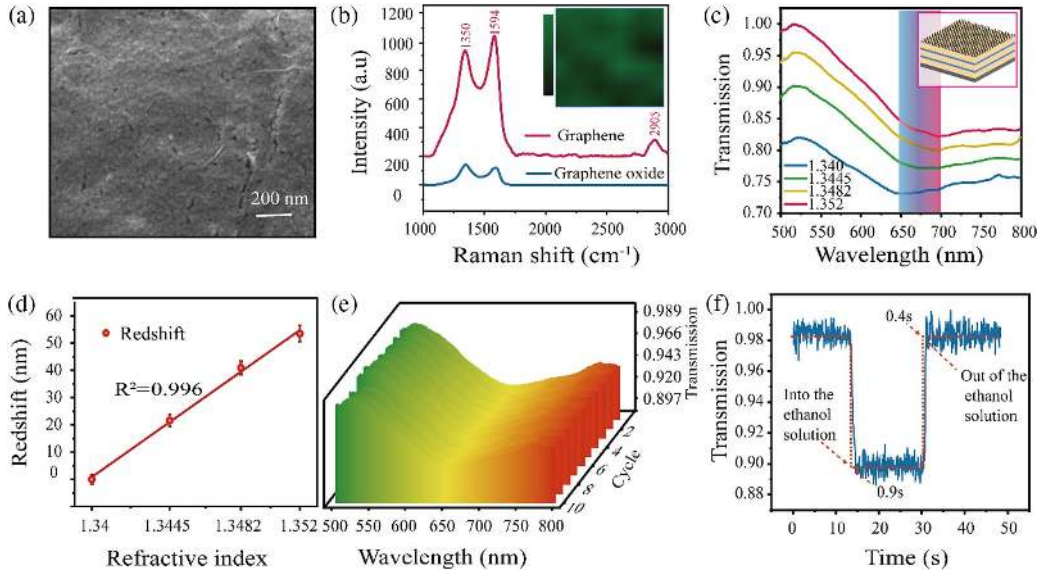

Fig. 6. (a) Front SEM image of G/HMM/D-POF in the sensing area. (b) Raman spectra of graphene oxide and chemically produced graphene. The inset shows the 2905 cm^{-1} peak position distribution within a scanned area of 20 μm × 20 μm. (c) Normalized transmission spectra of G/HMM/D-POF in the ethanol solutions with RIs from 1.340 to 1.352. (d) Resonance wavelength redshift of G/HMM/D-POF as a function of RI. (e) Normalized transmission spectra of G/HMM/D-POF at the RI of 1.352, recorded in a cycling mode (up to 10 cycles). (f) Typical response-recovery characteristic curve of G/HMM/D-POF in ethanol solution (RI of 1.352) at a resonance wavelength of 648 nm.

modification. Here, the transmission spectrum with the SPR peak wavelength of 647.75 nm, recorded from a sensor immersed in PBS solution with pH 7.4, was taken as the reference starting point. The entire modification of the PBASE on the surface of G/HMM/D-POF led to a resonance wavelength redshift of nearly 16.6 nm. This phenomenon is probably due to the p-doping effect caused by the charge transfer between the pyrene group and graphene. In turn, the interaction between the PBASE and the probe aptamer induced a redshift of 85.24 nm, owing to the electron-rich DNAs. Thus, the changes observed in the transmission spectrum during the two-stage process highlight the successful completion of the modification. For the analysis of the DNA binding, the normalized transmission spectra of the modified sensor in the t_DNA solutions with varying concentrations of 10 pM to 100 nM were collected after being sufficiently complementary to equilibrium [Fig. 7(b)]. Here, the transmission spectrum of a G/HMM/D-POF sensor modified with the probe aptamer in PBS solution (pH 7.4) was used as a reference starting point. The complete complementarity between the t_DNA and the probe aptamer brought a noticeable redshift in the resonance peak wavelength. The redshift, however, varied according to the t_DNA solution concentration. To a certain extent, the complementarity between the concentrated t_DNA solution and the probe aptamer could cause a pronounced change in the localized refractive index, thus resulting in a drastic redshift in the transmission spectrum. The variance in SPR redshifts during the measurement is displayed by a histogram in Fig. 7(c). In turn, the SPR wavelength versus t_DNA concentration is shown, as well. Obviously, it is well described with a straight line ($R^2 = 0.9948$), which proves its excellent capability of linear calibration. As seen, the SPR peak redshift value increases stepwise from 8.91 to 34.69 nm with rising t_DNA solution concentration from 10 pM to 100 nM. According to these data, the t_DNA detection limit of the sensor is nearly 10 pM.

To the specificity, the transmission spectrum was collected on the G/HMM/D-POF sensor immersed into a 1 μM mis_DNA solution. Figure 8(a) shows the normalized transmission spectrum of a sensor modified with probe aptamer in PBS solution and those after being replaced by a mis_DNA solution. In the entire time range for 22 min, the resonance wavelength was maintained at nearly 736.15 nm. Since no visual variations in the SPR resonance wavelengths were observed during the two stages, the local refractive index on the sensor surface remained unchanged, thus suggesting a non-bonding reaction between the probe aptamer and mis_DNA strands. Figure 8(b) illustrates the kinetics of DNA hybridization at different concentrations of t_DNA solutions in a cycle timing detection. Once the sensor is immersed in the t_DNA solution, there is the resonance peak redshift, reaching a plateau afterward. After reaching the plateau, the solution was replaced by a pure 0.01× PBS buffer solution to dissociate and remove target DNAs. In the entire cycle, t_DNA solutions were tested in a sequence of concentrations from 10 pM to 100 nM. The scatter diagram indicates that each individual association–dissociation cycle displayed a similar pattern. Before the DNA binding, the SPR redshift value was distributed within a shallow range tending to zero. Once the binding process was initiated, the redshift value increased rapidly until reaching a plateau and meaning the transition to the next stable state, followed by the dissociation. With increasing the dissociation degree, the redshift value was rapidly decreased, turning back to a shallow near-zero range and reaching the equilibrium again. The stepwise change in the SPR redshift value within a studied concentration region from 10 pM to 100 nM demonstrates the high resolution and outstanding repeatability of a sensor during a sequential DNA detection.

To a more specific analysis, a 0.1-nM DNA solution was proposed as a particular example. In this respect, Figs. 8(c) and 8(d) display the normalized transmission spectra recorded during the binding and dissociation processes, respectively. In Fig. 8(c), the SPR peak exhibits a noticeable redshift. The binding process occurs nearly 14 min before the dynamic equilibrium is attained, with only a slight deviation. After sufficient complementarity, the dissociation began. The SPR peak blueshifted with the dissociation and gradually returned to a pre-hybridization position, tending again to the dynamic equilibrium [Fig. 8(d)]. The DNA dissociation was ended by the 60-s immersion of a sensor in a 10-mM aqueous sodium hydroxide solution and its rinsing with PBS solution. The recovery of a resonance peak position at nearly 736.15 nm indicated the complete regeneration for the next binding experiment. As found out afterward, the PBASE and probe aptamer modified on a sensor surface were not washed away. Figure 8(e) summarizes the redshift data for the hybridization and dissociation processes. Here, the resonance peak wavelength before hybridization is taken as the reference point

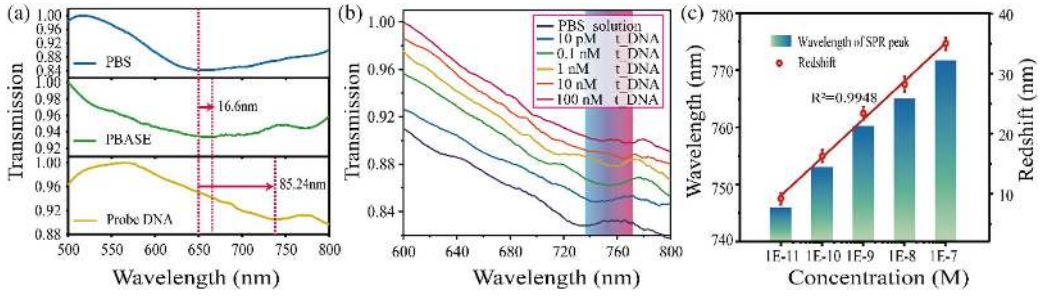

Fig. 7. (a) Normalized transmission spectra of the G/HMM/D-POF sensor during DNA modification. (b) Normalized transmission spectra of G/HMM/D-POF in t_DNA solutions with concentrations varying from 10 pM to 100 nM after being sufficiently complementary. (c) Redshift and SPR peak wavelength versus t_DNA concentration.

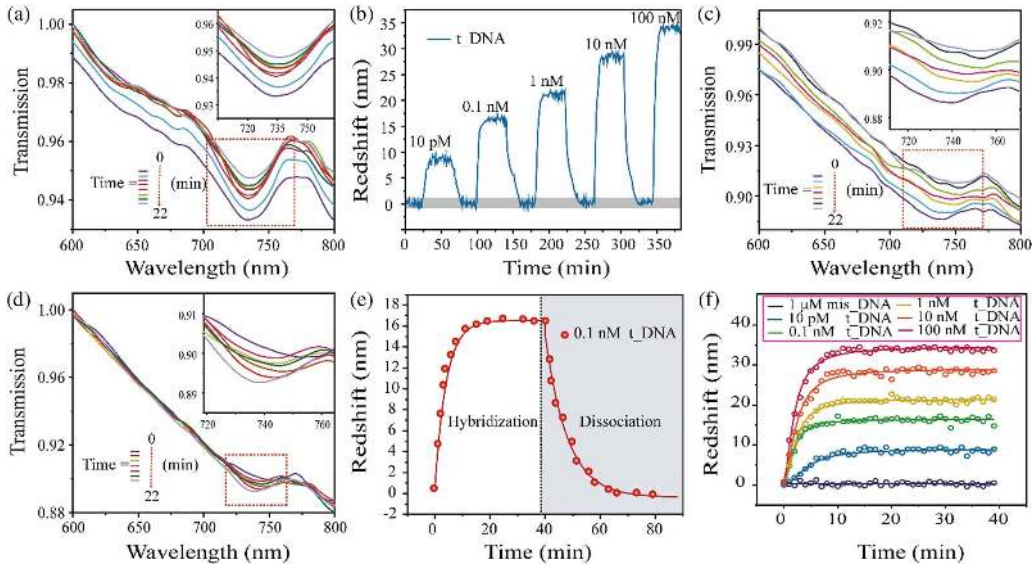

Fig. 8. (a) Normalized transmission spectra before and after adding mis_DNA. (b) Timing detection curve for t_DNA solutions with concentrations from 10 pM to 100 nM. (c) Normalized transmission spectra of G/HMM/D-POF in the 0.1 nM t_DNA solution during the binding process. (d) Normalized transmission spectra of G/HMM/D-POF in the 0.1 nM t_DNA solution during the dissociation. (e) Real-time redshift for the binding process and dissociation in the 0.1 nM t_DNA solution. (f) Real-time SPR wavelength shift for G/HMM/D-POF in mis_DNA and t_DNA solutions with concentrations from 10 pM to 100 nM.

and the entire variation in the SPR resonant wavelength appears as the time-dependent nonlinear curve. The process can be properly described with the Langmuir model [38]. The initial reaction speed of the binding process was the fastest. With the increasing density of the bonded molecules, the hybridization was gradually decelerated and eventually reached equilibrium. In turn, dissociation appears as a reverse reaction of binding. Furthermore, the resonance peak redshift curves associated with the DNA hybridization were compared at different solution concentrations (10 pM–100 nM) in the same time range. As shown in Fig. 8(f), the initial speed of the hybridization process increases with the concentration of the t_DNA solution. When the t_DNA and probe aptamer are sufficiently complementary, the density of the bonded molecules is associated with the t_DNA solution concentration. In other words, an increase in the t_DNA concentration increases the expected final density of binding.

Thus, the theoretical and experimental results obtained for a G/HMM/D-POF biosensor reveal its high-resolution capability, good linearity, fast response-recovery speed, and high-sensitivity DNA detection with a detection limit down to 10 pM for short DNA (15-mers).

4. CONCLUSION

An optical fiber SPR biosensor complying with a 3D Au/Al_2O_3 HMM composite structure and a graphene film was proposed in this study. According to a comprehensive theoretical and experimental analysis, the SPR resonance peak position could be able to be tuned within a visible-to-near-infrared range by altering the number of Au layers in the HMM system. Besides this, the sensor exhibited high sensitivity (4461 nm/RIU) and excellent linearity, as well as good stability and repeatability for bulk refractive index detection. Furthermore, according to the time- and concentration-dependent DNA hybridization kinetics data, the proposed sensor exhibited prominent performance with a detection limit of as low as 10 pM for short DNA (15-mers). These results made this appliance promising for a broad range of potential applications such as genetic screening, transcriptional profiling, biomarkers, and discovery of single-nucleotide variants. Thus, the combination of HMMs and 2D materials was shown to have great potential for SPR fiber optic sensors, making them promising for a broad range of medical diagnostics and clinical applications.

Funding. National Natural Science Foundation of China (11674199, 12074226, 12074229); Natural Science Foundation of Shandong Province (ZR2019MF025); Foundation of Shandong Provincial Key Laboratory of Biophysics (SD2019BP003).

Disclosures. The authors declare no conflicts of interest.

REFERENCES

1. H. Bhardwaj, G. Sumana, and C. A. Marquette, "A label-free ultrasensitive microfluidic surface plasmon resonance biosensor for Aflatoxin B1 detection using nanoparticles integrated gold chip," Food Chem. **307**, 125530 (2020).
2. H. H. Nguyen, J. Park, S. Kang, and M. Kim, "Surface plasmon resonance: a versatile technique for biosensor applications," Sensors (Basel) **15**, 10481–10510 (2015).
3. P. Singh, "SPR biosensors: historical perspectives and current challenges," Sens. Actuators B **229**, 110–130 (2016).
4. Q. Wang, J.-Y. Jing, and B.-T. Wang, "Highly sensitive SPR biosensor based on graphene oxide and staphylococcal protein A co-modified

TFBG for human IgG detection," IEEE Trans. Instrum. Meas. **68**, 3350–3357 (2019).
5. Y. Zhao, R. J. Tong, F. Xia, and Y. Peng, "Current status of optical fiber biosensor based on surface plasmon resonance," Biosens. Bioelectron. **142**, 111505 (2019).
6. E. N. Primo, M. J. Kogan, H. E. Verdejo, S. Bollo, M. D. Rubianes, and G. A. Rivas, "Label-free graphene oxide-based surface plasmon resonance immunosensor for the quantification of galectin-3, a novel cardiac biomarker," ACS Appl. Mater. Interfaces **10**, 23501–23508 (2018).
7. S. Nootchanat, W. Jaikeandee, P. Yaiwong, C. Lertvachirapaiboon, K. Shinbo, K. Kato, S. Ekgasit, and A. Baba, "Fabrication of miniature surface plasmon resonance sensor chips by using confined sessile drop technique," ACS Appl. Mater. Interfaces **11**, 11954–11960 (2019).
8. J. M. Pitarke, V. M. Silkin, E. V. Chulkov, and P. M. Echenique, "Theory of surface plasmons and surface-plasmon polaritons," Rep. Prog. Phys. **70**, 1–87 (2007).
9. X. Xi, J. Xu, S. Li, J. Song, W. Yang, Y. Sun, S. Jiang, Y. Han, and X. Fan, "An Au nanofilm-graphene/D-type fiber surface plasmon resonance sensor for highly sensitive specificity bioanalysis," Sensors (Basel) **20**, 991 (2020).
10. D. Zhang, G. Tan, M. Wang, B. Li, M. Dang, H. Ren, and A. Xia, "The enhanced photocatalytic activity of Ag-OVs-(0 0 1) BiOCl by separating secondary excitons under double SPR effects," Appl. Surf. Sci. **526**, 146689 (2020).
11. N. M. Y. Zhang, K. Li, P. P. Shum, X. Yu, S. Zeng, Z. Wu, Q. J. Wang, K. T. Yong, and L. Wei, "Hybrid graphene/gold plasmonic fiber-optic biosensor," Adv. Mater. Technol. **2**, 1600185 (2017).
12. H. K. Hunt and A. M. Armani, "Label-free biological and chemical sensors," Nanoscale **2**, 1544–1559 (2010).
13. M. Li, S. K. Cushing, and N. Wu, "Plasmon-enhanced optical sensors: a review," Analyst **140**, 386–406 (2015).
14. X. Xiong, Y. Chen, H. Wang, S. Hu, Y. Luo, J. Dong, W. Zhu, W. Qiu, H. Guan, H. Lu, J. Yu, J. Zhang, and Z. Chen, "Plasmonic interface modified with graphene oxide sheets overlayer for sensitivity enhancement," ACS Appl. Mater. Interfaces **10**, 34916–34923 (2018).
15. Y. Qian, Y. Zhao, Q.-L. Wu, and Y. Yang, "Review of salinity measurement technology based on optical fiber sensor," Sens. Actuators B **260**, 86–105 (2018).
16. X. D. Wang and O. S. Wolfbeis, "Fiber-optic chemical sensors and biosensors (2015-2019)," Anal. Chem. **92**, 397–430 (2020).
17. F. Chiavaioli, P. Zubiate, I. Del Villar, C. R. Zamarreno, A. Giannetti, S. Tombelli, C. Trono, F. J. Arregui, I. R. Matias, and F. Baldini, "Femtomolar detection by nanocoated fiber label-free biosensors," ACS Sens. **3**, 936–943 (2018).
18. Q. Wang, J.-Y. Jing, X.-Z. Wang, L.-Y. Niu, and W.-M. Zhao, "A D-shaped fiber long-range surface plasmon resonance sensor with high *Q*-factor and temperature self-compensation," IEEE Trans. Instrum. Meas. **69**, 2218–2224 (2020).
19. A. D. S. Arcas, F. D. S. Dutra, R. Allil, and M. M. Werneck, "Surface plasmon resonance and bending loss-based U-shaped plastic optical fiber biosensors," Sensors (Basel) **18**, 648 (2018).
20. N. Cennamo, G. D'Agostino, M. Pesavento, and L. Zeni, "High selectivity and sensitivity sensor based on MIP and SPR in tapered plastic optical fibers for the detection of l-nicotine," Sens. Actuators B **191**, 529–536 (2014).
21. Y.-N. Zhangd, E. Siyu, B. Tao, Q. Wu, and B. Han, "Reflective SPR sensor for simultaneous measurement of nitrate concentration and temperature," IEEE Trans. Instrum. Meas. **68**, 4566–4574 (2019).
22. N. Cennamo, F. Arcadio, A. Minardo, D. Montemurro, and L. Zeni, "Experimental characterization of plasmonic sensors based on lab-built tapered plastic optical fibers," Appl. Sci. **10**, 4389 (2020).
23. S. Deng, F. Yu, H. Deng, L. Yuan, and C. Teng, "Twisted tapered plastic optical fibers for continuous liquid level sensing," Opt. Fiber Technol. **59**, 102318 (2020).
24. L. Zeni, M. Pesavento, S. Marchetti, and N. Cennamo, "Slab plasmonic platforms combined with plastic optical fibers and molecularly imprinted polymers for chemical sensing," Opt. Laser Technol. **107**, 484–490 (2018).
25. W. Gong, S. Jiang, Z. Li, C. Li, J. Xu, J. Pan, Y. Huo, B. Man, A. Liu, and C. Zhang, "Experimental and theoretical investigation for surface plasmon resonance biosensor based on graphene/Au film/D-POF," Opt. Express **27**, 3483–3495 (2019).
26. G. Wang, Y. Lu, L. Duan, and J. Yao, "A refractive index sensor based on PCF with ultra-wide detection range," IEEE J. Sel. Top. Quantum Electron. **27**, 5600108 (2021).
27. W. Zheng, B. Han, E. Siyu, Y. Sun, X. Li, Y. Cai, and Y.-N. Zhang, "Highly-sensitive and reflective glucose sensor based on optical fiber surface plasmon resonance," Microchem. J. **157**, 105010 (2020).
28. A. Poddubny, I. Iorsh, P. Belov, and Y. Kivshar, "Hyperbolic metamaterials," Nat. Photonics **7**, 948–957 (2013).
29. S. A. Maier and H. A. Atwater, "Plasmonics: localization and guiding of electromagnetic energy in metal/dielectric structures," J. Appl. Phys. **98**, 011101 (2005).
30. S. Hu, Y. Chen, Y. Chen, L. Chen, H. Zheng, N. H. Azeman, M. X. Liu, G. S. Liu, Y. Luo, and Z. Chen, "High-performance fiber plasmonic sensor by engineering the dispersion of hyperbolic metamaterials composed of Ag/TiO_2," Opt. Express **28**, 25562–25573 (2020).
31. D. F. Santos, A. Guerreiro, and J. M. Baptista, "SPR optimization using metamaterials in a D-type PCF refractive index sensor," Opt. Fiber Technol. **33**, 83–88 (2017).
32. K. V. Sreekanth, A. De Luca, and G. Strangi, "Experimental demonstration of surface and bulk plasmon polaritons in hypergratings," Sci. Rep. **3**, 3291 (2013).
33. A. V. Kabashin, P. Evans, S. Pastkovsky, W. Hendren, G. A. Wurtz, R. Atkinson, R. Pollard, V. A. Podolskiy, and A. V. Zayats, "Plasmonic nanorod metamaterials for biosensing," Nat. Mater. **8**, 867–871 (2009).
34. K. V. Sreekanth, Y. Alapan, M. ElKabbash, E. Ilker, M. Hinczewski, U. A. Gurkan, A. De Luca, and G. Strangi, "Extreme sensitivity biosensing platform based on hyperbolic metamaterials," Nat. Mater. **15**, 621–627 (2016).
35. K. V. Sreekanth, Y. Alapan, M. ElKabbash, A. M. Wen, E. Ilker, M. Hinczewski, U. A. Gurkan, N. F. Steinmetz, and G. Strangi, "Enhancing the angular sensitivity of plasmonic sensors using hyperbolic metamaterials," Adv. Opt. Mater. **4**, 1767–1772 (2016).
36. C. Li, Z. Li, S. Li, Y. Zhang, B. Sun, Y. Yu, H. Ren, S. Jiang, and W. Yue, "LSPR optical fiber biosensor based on a 3D composite structure of gold nanoparticles and multilayer graphene films," Opt. Express **28**, 6071–6083 (2020).
37. J. Sun, S. Jiang, J. Xu, Z. Li, C. Li, Y. Jing, X. Zhao, J. Pan, C. Zhang, and B. Man, "Sensitive and selective surface plasmon resonance sensor employing a gold-supported graphene composite film/D-shaped fiber for dopamine detection," J. Phys. D **52**, 195402 (2019).
38. S. Xu, J. Zhan, B. Man, S. Jiang, W. Yue, S. Gao, C. Guo, H. Liu, Z. Li, J. Wang, and Y. Zhou, "Real-time reliable determination of binding kinetics of DNA hybridization using a multi-channel graphene biosensor," Nat. Commun. **8**, 14902 (2017).
39. W. Yang, J. Yu, X. Xi, Y. Sun, Y. Shen, W. Yue, C. Zhang, and S. Jiang, "Preparation of graphene/ITO nanorod metamaterial/U-bent-annealing fiber sensor and DNA biomolecule detection," Nanomaterials (Basel) **9**, 1154 (2019).
40. H. Neff, W. Zong, A. M. N. Lima, M. Borre, and G. Holzhüter, "Optical properties and instrumental performance of thin gold films near the surface plasmon resonance," Thin Solid Films **496**, 688–697 (2006).
41. R. Tabassum and B. D. Gupta, "SPR based fiber-optic sensor with enhanced electric field intensity and figure of merit using different single and bimetallic configurations," Opt. Commun. **367**, 23–34 (2016).
42. S. Tadepalli, Z. Kuang, Q. Jiang, K. K. Liu, M. A. Fisher, J. J. Morrissey, E. D. Kharasch, J. M. Slocik, R. R. Naik, and S. Singamaneni, "Peptide functionalized gold nanorods for the sensitive detection of a cardiac biomarker using plasmonic paper devices," Sci. Rep. **5**, 16206 (2015).
43. L. P. H. Jeurgens, W. G. Sloof, F. D. Tichelaar, and E. J. Mittemeijer, "Growth kinetics and mechanisms of aluminum-oxide films formed by thermal oxidation of aluminum," J. Appl. Phys. **92**, 1649–1656 (2002).
44. B. Wood, J. B. Pendry, and D. P. Tsai, "Directed subwavelength imaging using a layered metal-dielectric system," Phys. Rev. B **74**, 115116 (2006).

45. W. Yang, Z. Li, Z. Lu, J. Yu, Y. Huo, B. Man, J. Pan, H. Si, S. Jiang, and C. Zhang, "Graphene-Ag nanoparticles-cicada wings hybrid system for obvious SERS performance and DNA molecular detection," Opt. Express **27**, 3000–3013 (2019).
46. W. Zhou, J. Zhu, C. Cheng, J. Liu, H. Yang, C. Cong, C. Guan, X. Jia, H. J. Fan, Q. Yan, C. M. Li, and T. Yu, "A general strategy toward graphene@metal oxide core–shell nanostructures for high-performance lithium storage," Energy Environ. Sci. **4**, 4954–4961 (2011).
47. J. Sun, X. Xie, K. Xie, S. Xu, S. Jiang, J. Ren, Y. Zhao, H. Xu, J. Wang, and W. Yue, "Magnetic graphene field-effect transistor biosensor for single-strand DNA detection," Nano. Res. Lett. **14**, 248 (2019).
48. L. Ferrari, C. Wu, D. Lepage, X. Zhang, and Z. Liu, "Hyperbolic metamaterials and their applications," Prog. Quantum Electron. **40**, 1–40 (2015).
49. Y. Guo, W. Newman, C. L. Cortes, and Z. Jacob, "Applications of hyperbolic metamaterial substrates," Adv. OptoElectron. **2012**, 452502 (2012).
50. C. L. Cortes, W. Newman, S. Molesky, and Z. Jacob, "Quantum nanophotonics using hyperbolic metamaterials," J. Opt. **14**, 063001 (2012).
51. J. Elser, V. A. Podolskiy, I. Salakhutdinov, and I. Avrutsky, "Nonlocal effects in effective-medium response of nanolayered metamaterials," Appl. Phys. Lett. **90**, 191109 (2007).